Experimental Observations of Spot Radiative Ignition and Subsequent Three-Dimensional Flame Spread over Thin Cellulose Fuels

S. L. OLSON*

NASA Glenn Research Center, Mail Stop 5003-115, Cleveland, OH 44135, USA

T. KASHIWAGI

National Institute of Standards and Technology, Gaithersburg, MD 20899

and

O. FUJITA, M. KIKUCHI[†], and K. ITO

Division of Mechanical Science, Hokkaido University, Kita-13, Nisi-8, Sapporo 060-8628 Japan

Non-piloted radiative ignition and transition to flame spread over thin cellulose fuel samples was studied aboard the USMP-3 STS-75 Space Shuttle mission, and in three test series in the 10 second Japan Microgravity Center (JAMIC). A focused beam from a tungsten/halogen lamp was used to ignite the center of the fuel sample while an external air flow was varied from 0 to 10 cm/s. Non-piloted radiative ignition of the paper was found to occur more easily in microgravity than in normal gravity. Ignition of the sample was achieved under all conditions studied (shuttle cabin air, 21%–50% O_2 in JAMIC), with transition to flame spread occurring for all but the lowest oxygen and flow conditions. Although radiative ignition in a quiescent atmosphere was achieved, the flame quickly extinguished in air. The ignition delay time was proportional to the gas-phase mixing time, which is estimated by using the inverse flow rate. The ignition delay was a much stronger function of flow at lower oxygen concentrations. After ignition, the flame initially spread only upstream, in a fan-shaped pattern. The fan angle increased with increasing external flow and oxygen concentration from zero angle (tunneling flame spread) at the limiting 0.5 cm/s external air flow, to 90 degrees (semicircular flame spread) for external flows at and above 5 cm/s, and higher oxygen concentrations. The fan angle was shown to be directly related to the limiting air flow velocity. A surface energy balance reveals that the heat feedback rate from the upstream flame to the surface decreases with decreasing oxygen mass transport via either imposed flow velocity or ambient oxygen concentration. Quenching extinction occurs when the heat feedback rate from the flame is no longer sufficient to offset the ongoing surface radiative heat losses. Despite the convective heating from the upstream flame, the downstream flame was inhibited due to the 'oxygen shadow' of the upstream flame for the air flow conditions studied. Downstream flame spread rates in air, measured after upstream flame spread was complete and extinguished, were slower than upstream flame spread rates at the same flow. The quench regime for the transition to flame spread was skewed toward the downstream, because of the augmenting role of diffusion for opposed flow flame spread, versus the canceling effect of diffusion at very low cocurrent flows. © 2001 by The Combustion Institute

INTRODUCTION

Ignition of solid fuels by an external radiant heat source, and the subsequent transition to flame spread are both processes that have application to spacecraft fire safety. A material that undergoes a momentary ignition but quickly extinguishes might be acceptable for use in spacecraft, but a material which permits transition from ignition to flame spread poses a significant hazard and is clearly undesirable. Unfortunately, our fundamental understanding of what controls this transition is not well developed at this time.

A fire's hazard is determined by the total heat release rate from the fire. The total heat release rate depends on the burning area and the burning rate. Burning area depends on the flame's spread rate and spread pattern. Generally, a fire starts from a small local ignition source and spreads out three-dimensionally from there. The flame spread directionality is a strong function of the wind direction or buoyant flow direction. To assess a fire's hazard in spacecraft, it is important to un-

---
*Corresponding author. E-mail: sandra.olson@grc.nasa.gov
[†] Currently at National Space Development Agency of Japan, Tsukuba Space Center, Ibaraki, 305-8505 Japan.

derstand the likely flame spread pattern in a low speed flow microgravity environment.

Almost all previous works have studied ignition and flame spread independently. Previous radiative ignition studies [1, 2] were either one-dimensional or stagnation point geometries, where the mismatches between experiments and theory make direct comparison difficult. A recent two-dimensional axisymmetric model [3] with variable gravity (variable buoyant flow) predicts ignition at low gravity ($g < 0.2$ g_0, low buoyant flow) occurs at the fuel vapor plume cap, which is controlled by one-dimensional heat and mass transport processes.

Previous microgravity flame spread studies of thermally thin fuels found quenching extinction in quiescent air [4], and also found that 2D flame spread in air is a non-monotonic function of flow [5]. At elevated oxygen concentrations, 3D flame spread in quiescent atmospheres is symmetric about the ignition point, whereas if a wind is imposed across the sample, the flame propagates in a horseshoe shape, with the open side downstream of the ignition point [6]. 2D concurrent flame spread studies have found that spread rate increases monotonically with flow, but that steady state flame size is difficult to achieve in drop tower timescales or Shuttle Glovebox size constraints [7].

Previous detailed thin fuel flame spread computational studies [8–10] are generally steady-state and two-dimensional, so transient and three-dimensional effects are not described. Kashiwagi et al. [6] have developed a three-dimensional transient full Navier-Stokes model with finite rate chemistry and surface radiative loss that has been shown to model microgravity ignition and transition well.

There are still many outstanding issues in flame spread over thin fuels in a slow wind, especially at low oxygen concentrations where thermal theory is not valid [5]. The experiments described here are intended to shed light on slow wind effects on spot ignition in the center of the sample, the 3D flame transition from the localized ignition to spread, the 3D flame growth pattern and direction of propagation, and the heat feedback from the flame front to the surface. As will be shown, the heat and mass transport both strongly affect the flame shape and direction of propagation. Data obtained from this study will be available for comparison with theoretically calculated results to verify the model and also to understand the mechanisms of ignition and transition to flame growth.

HARDWARE

Radiative Ignition and Transition to Spread Investigation (RITSI) flight hardware consisted of the flow duct, a control box, and a display box. Parts boxes housed the individual sample boxes and other miscellaneous supplies. Astronaut experiment controls on the small external control box, included fan on/off and variable speed control, ignitor wire activation, radiant heater activation and variable power adjustment, and chamber light on/off and blinking. The engineering hardware, used in JAMIC testing, was automated using relays but was functionally equivalent.

The flow duct, shown schematically in Fig. 1, was 85 mm wide $\times$ 95 mm high $\times$ 171 mm long. The ambient environment to the flow duct was provided by an enclosure around the flow duct. In the shuttle experiments the ambient environment was cabin air (approximately 21% O_2) contained in the Middeck Glovebox working volume, whereas in JAMIC a sealed chamber was filled with the desired mixture (21, 35, 50% O_2 in N_2). The blue filter window lid of the duct opened for access to change out sample cards and replace a combustion products filter (molecular sieve, activated carbon, metal honeycomb, screens, and an electrostatic sub-micron particle filter). The 2.5 cm thick filter was downstream of the combustion event and collected particulates, absorbed many gaseous products, and served as the dominant pressure drop in the system and passive heat sink to maintain a constant temperature of the exhaust gases so that the volumetric flow through the fan remained constant throughout the experiment.

The slow flow velocity through the test section was generated by a small fan drawing air through the test section at speeds from 0 to 10 cm/s. Calibration of the fan voltage with the actual velocity of these low speed flows was performed in normal gravity using a low velocity hot wire anemometer to measure the velocity in

the reduced cross-sectional area in front of the fan. The test section flow was calculated from this using the ratio of the cross-sectional areas and the measured pressure drop between the measurement site and the test section. The probe was specially calibrated by the manufacturer for low speed flows, and the calibration was checked at the NASA Glenn Research Center against a fully developed pipe flow profile and a mass flow meter. Smoke flow visualization confirmed the smoothness of the flow through the test section. Within the flow duct, the presence of the flame locally perturbs the flow, but the primary pressure drop and heat sink in the flow duct is across the 2.5 cm thick packed bed combustion products filter just upstream of the fan, so the bulk flow through the test section remains constant.

A sample card is shown installed in the test section in Fig. 1. A 10 cm × 8.7 cm sheet of Whatman ashless filter 44 was used as the sample paper. A 1 cm grid was printed on each sample to aid in the analysis of results. The central section of the sample was blackened with a black Sharpie permanent marker to enhance absorption of the near-infrared radiation from the ignition lamp.

A near-infrared tungsten/halogen radiant heat lamp with a parabolic reflector was used to ignite the center of each sample. The lamp was recessed into the back wall of the flow duct and covered with a quartz window to minimize disturbances to the flow through the test section. The power to the lamp was measured during each test. The lamp automatically deactivated at a preset time. The total power output was calibrated as a function of input power with a flux meter, and the beam shape was characterized using a beam profiler. The beam was Gaussian, with a $1/e^2$ radius of 1 cm, at the sample surface, with a peak flux of 10 W/cm^2. The emission spectra of the lamp was measured from 2 to 20 μm by using a FTIR.

Six 0.05 mm diameter type K thermocouples were pre-installed on each sample with the beads on the centerline of the sample; four were sewn into the surface, and two were stretched across the sample two mm above the surface in the gas-phase. The thermocouple signals were cold-junction compensated, signal conditioned, and recorded along with radiant heater power, and flow velocity. No corrections have been made (radiation, conduction) to the thermocouple data.

Color video pictures were taken of the sample surface to observe changes in the flame shape and char pattern. Red diodes were used to illuminate the sample surface so the dim blue flame would still be visible. It was impossible to observe ignition with the video due to the bright light of the tungsten/halogen lamp used for ignition. Still color photographs were taken at an oblique angle by a motor-driven 35 mm camera to image the flame spread, char and smoke patterns.

IGNITION

In normal gravity, the irradiation from the lamp was insufficiently energetic to ignite the quickly convected hot degradation products in either horizontal or vertical orientations. A heated pilot wire placed in the gas phase above the irradiated surface was needed to ignite the degradation products. The ignition occurred in the gas-phase, and if no gas-phase pilot was present, the lamp would simply vaporize a hole through the material with no additional reaction [11]. The buoyant convection cooled and removed the fuel vapors before they have a chance to mix with oxygen, heat up and ignite.

However, in microgravity a gas-phase pilot was not needed. The irradiation from the lamp alone was sufficient to ignite the samples. Thus, this material was more readily ignited by external radiant sources in microgravity. This may be because the pyrolysis vapors remained within the lamp irradiated spot for long enough to mix with the oxidizer and absorb sufficient radiant energy or to be heated to sufficient temperatures by the hot charring surface to achieve ignition without the aid of a pilot. At ignition, the cloud of fuel vapor ignites and the flame stabilizes over the ignition point, as shown in Fig. 2. In the JAMIC testing, an on-board microphone easily detected the distinct sound of the thermal expansion wave of ignition.

The ignition delay time is defined as the time from the first detected sample heating above ambient to ignition of the sample. This definition eliminates a hardware specific 1.2 s lag time from ignition activation to the first detected sample heating, making the results more useful
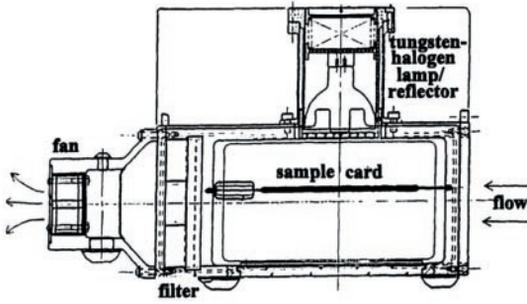
(a)

(b)

Fig. 1. a) Schematic of RITSI experiment module. Flow is drawn through the test section by a small fan. A tungsten-halogen lamp and reflector are recessed in the duct wall, and irradiate the center of the sample. The combustion products are filtered before exiting the test section. b) Photograph of the RITSI flight hardware with sample card and filter installed, with interface cables, control box and digital display box.
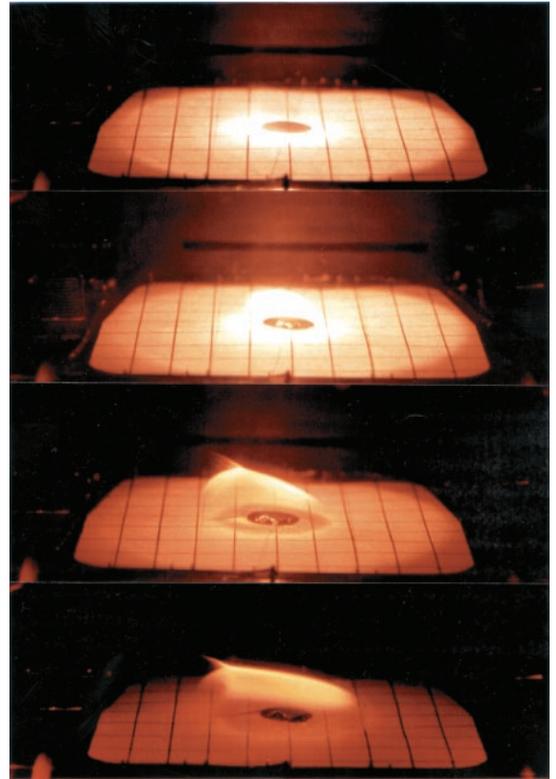

Fig. 2. A large flame plume develops quickly during radiative ignition of a paper sample via near-infrared radiation in a 50% oxygen, 5 cm/s flow environment. Images are approximately 0.8 s apart. Grid on paper is 1 cm square. a) faint fuel vapor dome-shaped cloud forms over the irradiated spot, b) ignition "cap", c) and d) transition from ignition to flame spread as the ignition "cap" expands and begins to spread across the sample.

for future comparisons. The ignition delay time was determined from the digital data, which provided thermocouple data throughout the test. Ignition is quite energetic; the thermal expansion wave from the ignition event easily exceeds the imposed flow and is quickly sensed by the thermocouples both upstream and downstream of the ignition spot.

The ignition delay time was linearly dependent on the inverse flow velocity for air/21% and 35% oxygen over the range of flow conditions studied, as shown in Fig. 3. The inverse flow velocity is proportional to the gas-phase or mixing time, which is the time needed to develop a flammable mixture of the slow-flowing

air and pyrolyzing fuel. The slower the flow, the longer the ignition delay time. The slope of the ignition delay time-inverse flow velocity curve was roughly 1/2. The slope can be considered to be a gas-phase characteristic length scale in cm, and agreed quantitatively with the radius of the heated spot. Thus the gas-phase residence time over the heated spot is a critical parameter in ignition delay—the fuel-oxygen mixing and mixture heat up occur during this time above the heated spot.

Ignition delay times were shorter at higher oxygen concentration, consistent with trends predicted in [12]. The effect of flow velocity on the ignition delay time in 50% oxygen were less than at lower oxygen concentration. The influence of flow velocity became more pronounced at lower oxygen concentrations, as shown in the
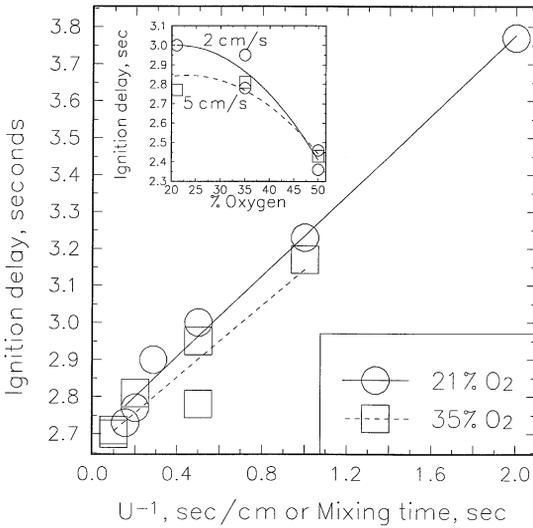
Fig. 3. Ignition delay times are linearly dependent on the inverse of the imposed flow, which is a residence or mixing time for a given irradiated spot size and power level. Inset shows the ignition delay dependence on oxygen concentration for two different flow rates, 2 and 5 cm/s.

inset to Fig. 3 where ignition time was plotted against oxygen concentration for two different flow velocities. At high initial oxygen concentrations, the rate controlling step for ignition was surface heat up (~2.1 s to reach 430°C ± 30°C, from thermocouple data for all flow and O_2 levels), and the gas-phase mixing/reaction occurs within a few tenths of a second after the fuel surface reaches pyrolysis temperatures (for all flows studied, but at low oxygen concentrations, the portion of the ignition delay in Fig. 3 associated with this gas-phase mixing/reaction ($t_{ign} - 2.1$ s) agrees closely with the flow-based mixing time for the 1 cm diameter spot.

FLAME SPREAD

Flame spread from a central ignition spot is unique in that the flame in this situation can go in whatever direction(s) it finds conducive to spread. The resultant flame spread patterns not only reveal the important controlling mechanisms for the flame spread but also provide information about the fire hazard in a realistic fire scenario.

Transition to flame spread was achieved for all flow velocities tested with the exception of the quiescent air case, where ignition was fol-

lowed by a quenching extinction. This flame spread extinction limit was expected based on previous work with a thinner fuel [4]. However,
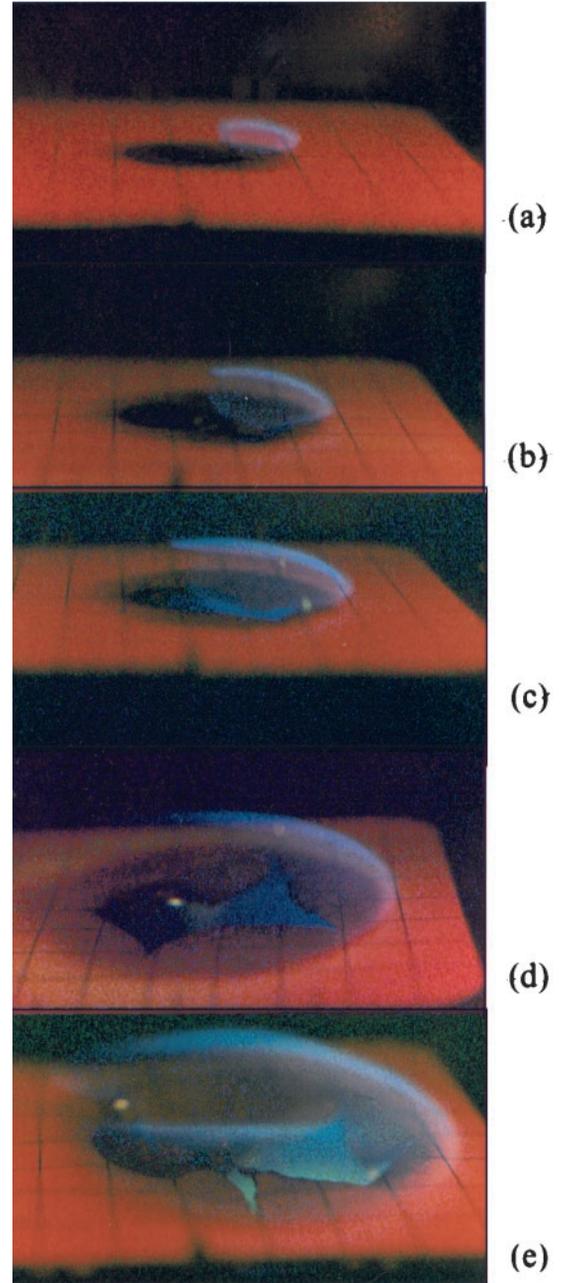

Fig. 4. 35 mm still photographs showing an oblique view of the surface of the sample as the flame spread approaches the upstream edge of the sample for different air flow rates. Flame is blue over charring sample, which is illuminated by red LEDs. Air flow is entering from the right. a) 0.5 cm/s, b) 2 cm/s, c) 3.5 cm/s, d) 5 cm/s, e) 6.5 cm/s.
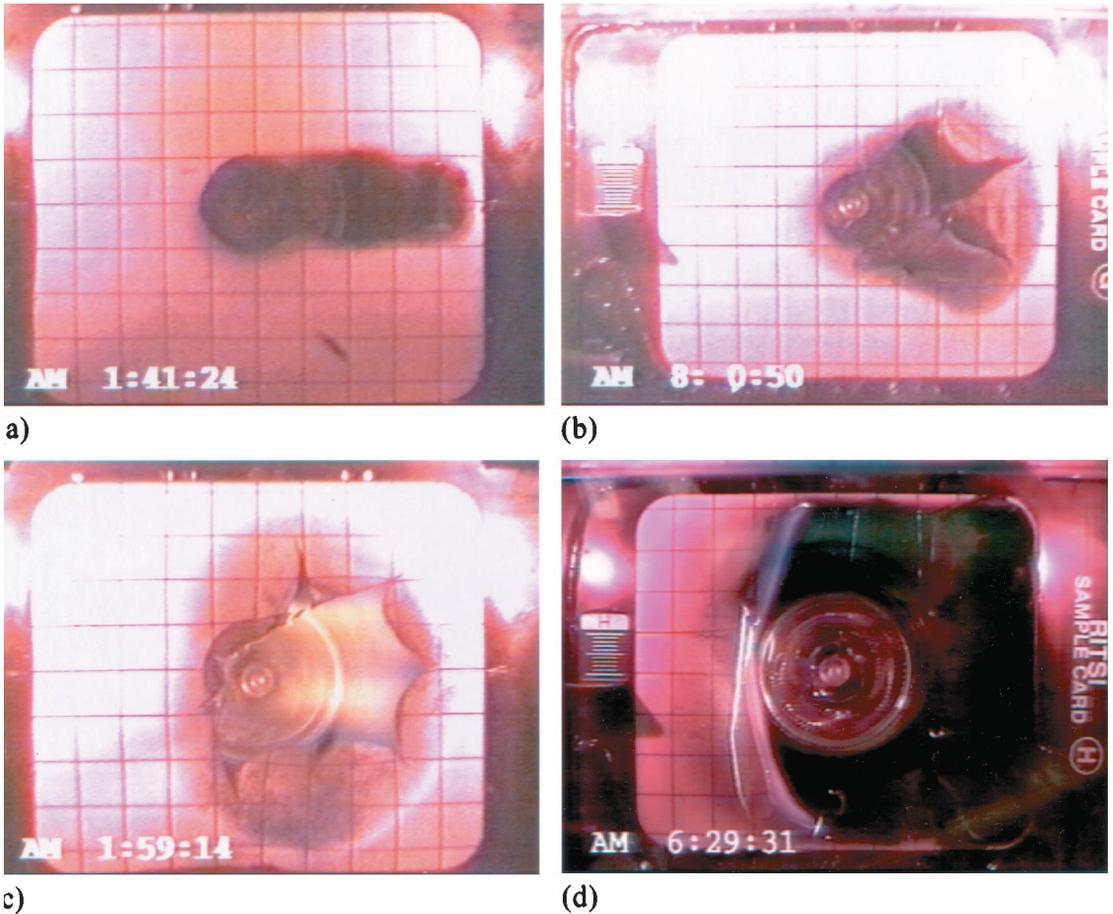
Fig. 5. Video stills showing surface view of the sample illuminated with red LEDs during tests with different flows. Grid on sample surface is 1 cm square. (a) tunneling flame spread into 0.5 cm/s flow. Flame is unable to spread laterally and tunnels straight into the fresh oxidizer flow. Downstream flame spread does not occur at this flow rate. (b) fan-shaped flame spread into 2 cm/s flow. Flame is able to fan out more with increasing flow. Lamp is visible through burned hole in the paper, and large cracks in the charred sample are observed. (c) semi-circular flame spread into 6.5 cm/s flow. Some sooting is apparent at this highest flow studied. Cracks are again apparent, with a large hole in the sample. Simultaneous downstream flame spread was not observed over the range of flows studied (0.5–6.5 cm/s). (d) concurrent (downstream) flame spread with 5 cm/s flow. Once the upstream flame spread was complete, the flame wrapped back around to the unburned downstream sample and a purely cocurrent flame spread is observed. Glowing white lines are thermocouples. Downstream flame spread consumed the entire downstream sample for imposed flows of 2 to 6.5 cm/s. The weaker flows of 0.5 and 1 cm/s had self-extinguishing downstream flames.

even for a very weak imposed air flow velocity of 0.5 cm/s, the transition to upstream flame spread was successful, so microgravity flames are very sensitive to very low velocity flows.

Simultaneous upstream and downstream flame spread in air was not observed over the range of flow studied to date. Downstream flame spread did not occur until the upstream flame spread was complete. Thus, the data presented can be considered opposed and concurrent flame spread.

Upstream (Opposed Flow) Flame Spread

The flame spread direction and rate were clearly dependent upon flow velocity. After ignition, the flame spread in only the upstream direction for air flows up to 6.5 cm/s, as shown in the oblique views of Fig. 4 and the direct surface views in Fig. 5 for flames in air. Upstream flame spread rates are measured by tracking the upstream char front position as a function of time. The upstream spread rates are very steady.
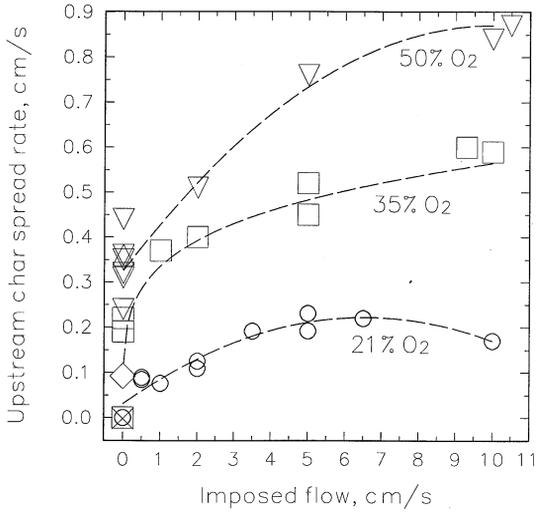
Fig. 6. Upstream flame spread rates for three different oxygen concentrations as a function of flow. ▽–50% O₂, □–35% O₂, ○–21% O₂, △–50% O₂ [13], ◇–35% O₂ [13], X–extinguished.
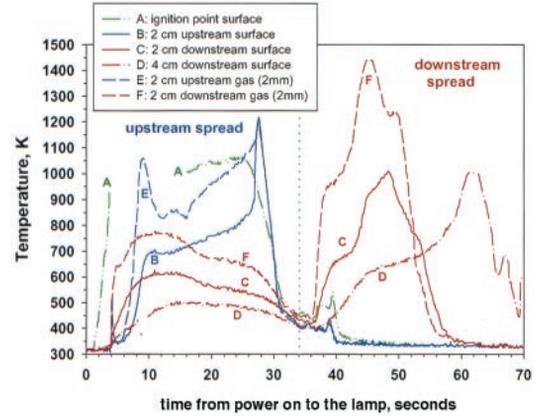

Fig. 9. Temperature history for a 5 cm/s imposed air flow experiment. The first 35 s is upstream (opposed flow) flame spread, while the next 35 s is downstream (concurrent) flame spread. Surface pyrolysis occurs at 700 K. Gas-phase flame temperatures reach as high as 1450 K.

Upstream flame spread along the centerline of the sample as a function of flow velocity is plotted in Fig. 6 for the three oxygen concentrations studied. The only other existing data [13] for ashless filter paper are in good agreement, as shown in Fig. 6. For all oxygen concentrations studied, the spread rate initially increases with flow velocity, but appears to be asymptotically approaching a maximum or plateau, which are the expected trends based upon previous microgravity results for two dimensional flame spread over thin fuels [4, 5], both in terms of the spread rate—flow velocity trends and the transition to a thermal regime of flame spread occurring at higher oxygen for this thicker fuel. Thus, it appears that the flame spread rate with respect to wind velocity is not significantly affected by the difference between 2D and 3D along the centerline except near quiescence, where data scatter becomes larger. The quenching region might be narrower for 3D geometries than for 2D configurations, which is predicted by calculation [12].

Downstream (Concurrent) Flame Spread

Despite convective heating, as will be shown by the thermocouple measurements discussed later, the downstream flame region was not simultaneously viable due to the 'oxygen shadow' cast by the upstream blue flame [6]. The incoming oxidizer was consumed by the upstream flame, and the combustion products from that flame vitiated the downstream flow. The downstream flame, unable to obtain sufficient oxygen in the vitiated flow, could not propagate while the upstream flame was present.

Once the upstream sample was consumed, however, the flame wrapped back around along the unburned lateral edges of the sample and a concurrent flame, able to obtain un-vitiated oxidizer flow, began to spread over the pre-heated downstream part of the sample. An image of concurrent flame spread is shown in Fig. 5d. The most difficult aspect of interpreting these flames is that they started from very non-planar initial conditions, as the flames wrapped around the burned edges remaining from the upstream propagation. The material is also preheated by the upstream flame (as much as 100 K from thermocouple data at 5 cm/s), which should enhance the flame spread.

Downstream flame spread measurements were made for the space experiments in air during this second phase of the test. In the JAMIC tests, there was insufficient time (10 s) to observe any downstream flame spread. Downstream flame spread rates were measured by tracking the char burnout point as a function of time. For downstream measurements, the

motion of the most upwind part of the flame—the flame base—was tracked. Good linearity of the flame base position versus time was obtained for periods of at least 25 s, and up to 100 s in the slower spreading cases. These times should be sufficiently long to reach steady state (estimated to take 16 s [14]).

Downstream flame spread was very sensitive to the flow velocity. For the 0.5 cm/s flow velocity test, the flame spread only along the burned sample free edges left by the upstream flame spread, completely unable to propagate directly downstream. The flames extinguished after spreading at most a few cm along the free edge. At 1 cm/s flow, while the flame was able to propagate downstream for a number of centimeters (for 100 s), it also frequently moved only along the burned edges. It quenched well before reaching the downstream edge of the sample, leaving unburned sample, and is thus considered to be self-extinguishing. Before extinction, it also exhibited a few 'flashes,' which are believed to be of a similar nature to the pre-extinction oscillations observed in candle flames in microgravity [15]. At 2 cm/s flow velocity, however, a cocurrent flame remained viable and the entire sample was consumed. A concurrent extinction limit thus appears to be between 2 cm/s and 1 cm/s imposed flow. This is of the same magnitude as diffusive velocities [4], so it is possible that a forced flow sufficient to overcome diffusion (of vitiating combustion products) is necessary for viable concurrent flame spread.

Comparing Upstream and Downstream Flame Spread Rates in Air

The upstream and downstream flame spread rates measured for air are plotted in Fig. 7, where upstream flows are positive and downstream flows are negative. The quench region observed in the experiments is indicated in Fig. 7, generally centered around quiescence but skewed to the downstream side, indicating that for very low speed flows, the upstream flame spread is the only viable option for a burning material. The slopes of the least squares regression fits for upstream and downstream spread rates with flow in Fig. 7 are the same to within the error of the measurement. These spread
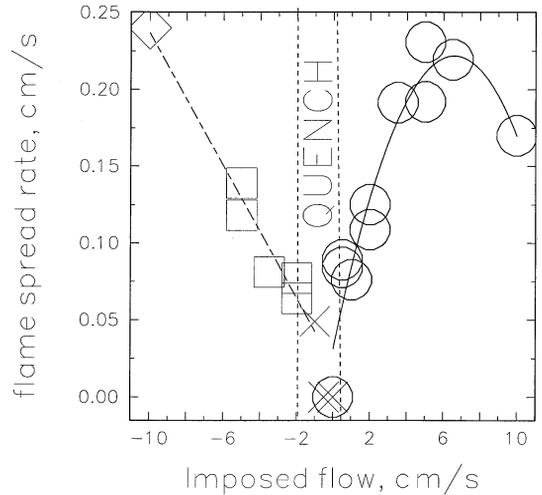

Fig. 7. Flame spread rates measured for both upstream (○–opposed flow) and downstream (□, ◇ [16]–concurrent) flames in air. Symbols are sized to estimate the error in the measurement. A quench region is indicated for flow velocities for which flames cannot be sustained in air (X–self-extinguishing).

rate trends are in excellent agreement with predictions [10, 12], even the expected peak [5, 12] in the upstream flame spread rate. Previous microgravity experiments over a thinner material [5] found the peak in spread rate for the thinner material at higher imposed flows (15–20 cm/s), so the peak spread rate may be a function of material thickness. The only other available microgravity slow wind datum with ashless filter paper [16] at 10 cm/s is also shown in Fig. 7, and agrees very well with the data from this work. The data also fit quantitatively with the spread rates noted in normal gravity experiments by Hirano and Sato [17] at higher flow rates for both concurrent and opposed flow.

Upstream (opposed-flow) flame spread is faster than downstream (concurrent) flame spread for a given flow, opposite to that concluded by Grayson et al. [7] who compared their results to those in [4]. However, we noticed the concurrent data in air and 30% in Grayson et al. [7] is slower than opposed flow data in [5]. This trend of faster upstream flame spread is the exact opposite of normal gravity flame spread where not only is simultaneous upward (downstream) and downward (upstream) flame spread possible, but the downstream flame is much faster than the upstream flame. It is expected
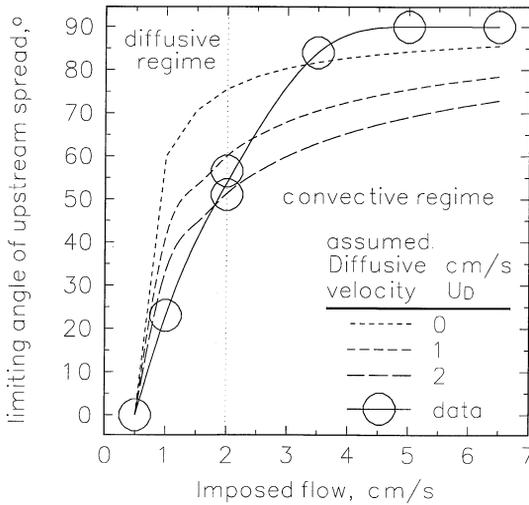
Fig. 8. A comparison between the measured flame angles in air and the angle estimated using Eq. 3. Diffusive velocities need to be accounted for when imposed flows are of the same magnitude.

that at sufficiently high forced flow, that simultaneous upstream and downstream flame spread will become viable. It is also likely that downstream flame spread will continue to accelerate with increasing flow velocity to merge with the known high flow velocity flame acceleration trends [17] whereas the upstream flame spread will peak and then begin to fall off with increasing flow [5].

3D LIMITING FLAME ANGLES

As mentioned above, during the early part of all tests, the flame spread (when it occurred) was solely upstream diverging from the ignition region. However, for tests in air there appears to be a maximum angle of flame spread for a given flow, which can be seen in the char patterns in Fig. 5. The experimental angle, defined as the angle from the ignition spot to the upstream lateral edges of the char region as the upstream flame neared the upstream edge of the sample, was measured from the video images. The measured angles for the long duration USMP-3 tests in air are shown in Fig. 8 as a function of flow velocity. At sufficiently high flow velocities (>3.5 cm/s), the flame angle is nearly 90 degrees, indicating semicircular flame propagation in the upstream direction. Below that flow rate, however, the flame angle reduces with flow rate

until a limit of zero angle is reached at 0.5 cm/s flow. The flame at 0.5 cm/s air flow rate propagated directly upstream without any lateral growth. A quiescent case extinguished shortly after ignition, so the 0.5 cm/s flow rate case is very near the extinction limit.

A simple analysis that estimates the air flow normal to the flame front to determine the limiting flame angles is compared here with the measured results. The component of the flow velocity normal to the curved flame front, U_n, is estimated from geometric considerations to be

$$U_n = U_\infty \cos \alpha \tag{1}$$

where α is the maximum flame angle and U_∞ is the free stream flow velocity. We also know, from the experiments, that the limiting air flow velocity for upstream flame spread was very close to $U_{n,\mathrm{lim}} = 0.5$ cm/s, where the flame spread angle for the tunneling flame was zero. If we solve Eq. 1 for the limiting angle at which the normal air flow velocity becomes the approximate limiting value of 0.5 cm/s, we obtain

$$\alpha = \cos^{-1}(U_{n,\mathrm{lim}}/U_\infty) \tag{2}$$

However, for very weak imposed flows, the diffusive velocity, U_D, cannot be neglected as a source of oxidizer transport. The magnitude of U_D has been estimated to be 1 to 2 cm/s [4]. If we use linear superposition to incorporate this effect, Eq. 2 becomes

$$\alpha = \cos^{-1}[(U_{n,\mathrm{lim}} + U_D)/(U_\infty + U_D)] \tag{3}$$

Curves of this equation are shown in Fig. 8 for values of U_D of 0 and 2 cm/s along with the actual angle measured in each test. Qualitative agreement is obtained at the higher flow rates (convective regime) when diffusion is neglected ($U_D = 0$). However, the importance of diffusion is pronounced for the flows at and less than 2 cm/s (diffusive regime), where qualitative agreement is obtained only when a $U_D = 2$ cm/s is used. Simply using the air flow velocity normal to the flame front is sufficient to qualitatively predict the trend in the limiting spread angle if the extinction limit flow velocity value is known. By using the same expression, it is possible to estimate the extinction limit flow velocity using an experimentally measured flame spread angle for a given material.

TEMPERATURE MEASUREMENTS

The temperature data recorded in each test provide a more detailed picture of events. Figure 9 (see page 858) shows the temperature traces from a 5 cm/s flow test, which is almost two independent experiments for the upstream and downstream flame spread portions of the test. The ignition point surface temperature shows the rapid heating from the radiant heater at the ignition point with only a slight inflection at the pyrolysis temperature of about 700 K as the sample quickly degraded due to the intense radiant heat. Ignition occurs in the gas-phase at approximately 4 s (including a 1.2 second lamp lag time described in the Hardware section), as indicated by the spikes in the upstream traces and rapid rise in the downstream thermocouple traces. The spikes in the upstream thermocouples indicate that the thermal expansion of ignition was stronger than the incoming flow, but that the flow then quickly (<1 s) washed the remnants downstream in the 5 cm/s flow. In contrast, the downstream thermocouples show a steady rise due to convective heating from the upstream flame.

The upstream flame passed the 2 cm location at 9 s after ignition with a peak gas-phase temperature (2 mm above the surface) of nearly 1100 K beneath the leading edge of the flame, and a surface pyrolysis temperature following 1.5 s later of 700 K. By using the steady upstream centerline spread rate of 0.23 cm/s, the 1.5 s corresponds to 0.35 cm of flame overhang ahead of the pyrolysis front. The tail of the upstream flame passes at 28 s (6.5 cm), with peak temperatures of 1200 K both in the gas and at the burned out surface location. Temperatures fall precipitously at 30 s when the upstream flame burns out as it reaches the upstream edge of the sample.

The downstream thermocouple history is also interesting. After ignition, the downstream thermocouples quickly heat up due to convective heating from the upstream flame. Surface temperatures of 625 K are recorded at 2 cm downstream from the ignition point, while 2 mm in the gas phase at that same location temperatures reach almost 800 K. This surface temperature is very close to the onset of pyrolysis for cellulose, so, for higher flow rates with in-creased convective heating, it is likely that simultaneous downstream flame spread will be viable as oxygen also becomes more available with increased convection. Even at 4 cm, the downstream surface temperatures reach 500 K. As the upstream flame moves further away from the downstream thermocouples, the temperatures fall gradually. When the upstream flame extinguishes at 30 seconds, all temperatures drop to approximately 450 K as the flame makes its way back around the periphery of the burned material to the unburned downstream material. At 35 s, the flame begins to spread downstream, and temperatures at 2 cm downstream of the ignition point quickly heat up to 950 K in the gas-phase beneath the flame tips, and 700 K as the fuel begins to pyrolyze. The flame base passes over the thermocouple location at 48 s, with a peak gas-phase temperature of 1450 K, and 1000 K at the burned surface. The 4 cm surface thermocouple shows an extended pre-heat region but otherwise is very similar to the 2 cm downstream surface thermocouple. The distance between the two peaks (2 cm) divided by the time between peaks (13 s) agrees very well with the visually tracked spread rate for this test.

Upstream preheat lengths were all approximately 3 to 4 mm in length to within the error in the measurement, as determined from the visual distance between the blue flame leading edge and the pyrolysis front beneath the flame on the paper surface. Downstream pyrolysis lengths were measured during downstream flame spread in air that occurred after the upstream flame spread was complete. Pyrolysis lengths (0.6–2 cm) were determined from the distance between the initial visible darkening of the sample and the burnout point, and grow linearly with imposed flow, as does the concurrent spread rate. There is thus a linear relationship between pyrolysis length and flame spread rate for downstream flame spread.

HEAT FLUX ANALYSIS

The temperature-time data were used in a simple surface balance in the preheat region of the flame during upstream flame spread. The surface balance equates the heat feedback rate from the overhanging upstream flame with the

fuel heat up and re-radiation. This model focuses on the preheating feedback flux from flame until pyrolysis temperatures, or so-called ignition temperatures, are achieved. Because the overall effect of the cellulose degradation is only slightly endothermic [18, 19], it is neglected in this analysis. This energy balance provides a simple method to evaluate the heat feedback rate from the leading edge of the flame to the surface. From this balance we can determine the peak heat flux as a function of oxygen mass transport (via external flow velocity and O_2 concentration). The surface balance used is as follows:

$$q''_{feedback} = \rho_s \tau C_s \frac{\partial T_s}{\partial t} + \epsilon\sigma(T_s^4 - T_\infty^4) \qquad (4)$$

where the half thickness area density $\rho_s\tau = 0.00385$ g/cm^2, emissivity $\epsilon = 0.85$, Stefan–Boltzmann constant $\sigma = 5.729 \times 10^{-12}$ W/cm^2 K^4, heat capacity $C_s = 1.26$ J/g K, and ambient temperature $T_\infty = 300$ K. The first derivative of the temperature-time data was taken by using a Savitsky–Golay differentiation scheme, with 13 surrounding points. Time was converted to distance using the measured spread rate, and linearly shifted so that $x = 0$ at the leading edge. The peak heat flux is usually noted as the leading edge of the flame passes the thermocouple location ($x = 0$). However, for the weakest flames, the leading edge heatup flux is small and the preheat lengths are long. This results in low surface re-radiation at the leading edge, so that the peak heat flux to the surface does not occur until after the leading edge of the flame has passed. After passage of the flame leading edge, the surface reaches an approximately constant pyrolysis temperature, but surface radiative loss is significant, so the heat feedback rate from the flame to the surface plateaus at approximately 1.3 W/cm^2 until burnout.

Figure 10 shows the peak heat feedback rate from the flame dependence on imposed flow for the three oxygen levels tested. The dependence is not quite linear, with increasing levels of heat flux with increasing imposed flow velocity as the flame is pushed closer to the fuel surface. Increasing the oxygen concentration also increases the heat flux due to higher flame temperatures. The slopes of the heat flux-flow data
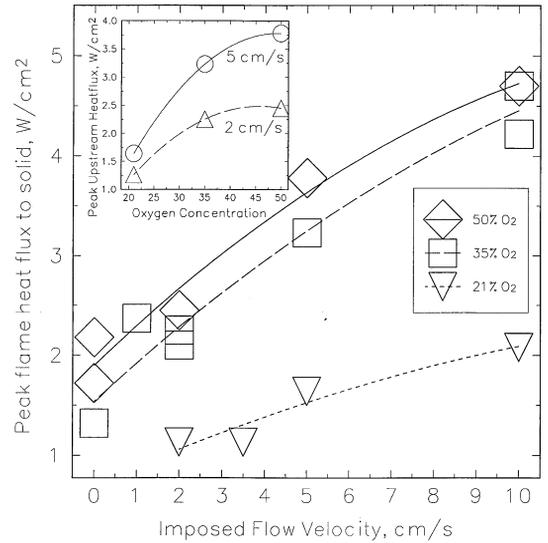

Fig. 10. Peak heat flux from the upstream flame to the surface at the thermocouple location as a function of imposed flow for three oxygen concentrations. The inset to the figure presents the oxygen dependance of the peak heat flux for two imposed flow velocities.

for 35% and 50% are nearly identical, but the near limit atmosphere of air shows a lower slope. The inset to Fig. 10 provides a clearer picture of the peak heat flux dependence on oxygen concentration for two different flow velocities. The dependence is nonlinear, and falls off sharply at lower oxygen levels. The peak heat flux levels for air are marginally higher than re-radiation loss levels.

Another way to interpret the importance of the surface balance is by comparing relative terms in the surface balance above. Here we define the fraction of radiatively-lost heat feedback rate to be

$$F_{loss,\, leading\, edge} = \frac{\epsilon\sigma(T_{s,\, leading\, edge}^4 - T_\infty^4)}{q''_{feedback,\, leading\, edge}} \qquad (5)$$

This is the fraction of the heat flux from the leading edge of the flame that is needed to counteract the surface re-radiative loss beneath the leading edge of the flame. The remaining fraction of the heat flux from the leading edge flame is then available for fuel heat up, according to the surface balance. Obviously, if the F_{loss} approaches unity, the flame is barely able to offset radiative losses even beneath the not-yet pyrolyzing fuel, and the flame is very close to
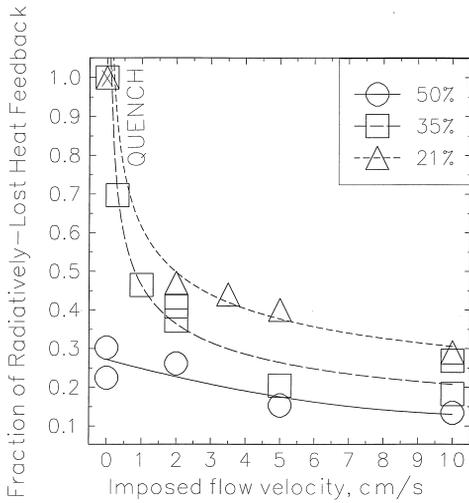
Fig. 11. The fraction of the upstream heat flux from the leading edge of the flame that is lost to surface radiation as a function of imposed flow for three oxygen concentrations. The fractional heat losses increase at low flow at the lower oxygen concentrations due to the decreasing heat feedback rate from the leading edge of the flame, while the radiative losses remain almost constant. Quenching extinction is noted when the fractional losses become too great.

extinction. The radiative losses themselves remain fairly constant; near extinction the heat feedback from the leading edge of the flame is almost too low to offset the losses, due to low oxygen supply to the flame.

The calculated F_{loss} dependence on imposed flow velocity is shown in Fig. 11. For 50% oxygen, the fractional losses remain below 30% over the range of flow rates, so the flame is quite robust even for the lowest flows. At 35% and 21% oxygen, however, as flow decreases the fractional losses increase dramatically, and for quiescent conditions quenching is noted shortly after the fractional heat loss of 70% is observed (35% oxygen quench extinction data). Fractional heat losses increase with decreasing oxygen for any given flow rate. As was shown in Fig. 10, the fractional losses are increasing at low flow because of the decreasing heat feedback rate from the leading edge of the flame, whereas the radiative losses remain almost constant. Quenching extinction is noted when the peak heat feedback rate from the flame to the surface is no longer sufficient to offset the ongoing losses, which is estimated to be when heat loss exceeds 70% of the peak heat flux.

CONCLUSIONS

This experiment is the first to examine non-piloted radiative ignition of a material in microgravity. Ignition occurred more readily in microgravity than in normal gravity. This is believed to be because the hot pyrolysis vapors remained within the lamp irradiated spot for long enough to mix with the incoming oxidizer and heat up to the ignition temperature without the aid of a pilot. For 21% and 35% oxygen concentrations, the ignition delay time is linearly dependent on the gas-phase residence/reaction time, which is inversely proportional to the imposed flow velocity. The flow mixing time is not significant at 50% O_2, where solid-phase heatup dominates the ignition delay time.

This experiment is also the first to look at the flame spread preferences of a centrally ignited flame in a weakly ventilated microgravity situation. In this experiment, the initial flame spread occurred only in the upstream direction, indicating its strong need for fresh oxidizer. The upstream flame spread dependence on flow velocity for lower oxygen concentrations is consistent with previously reported results [4, 5].

The angle of the flame as it spreads upstream is shown to be a function of the flow velocity. A simple analysis that estimates the limiting air flow normal to the semicircular flame front to determine the limiting flame angles is shown to agree qualitatively with the measured results.

A simple surface balance was used to determine that while the heat losses remain nearly constant (~1 W/cm^2), the heat feedback rate from the upstream flame to the surface is a strong function of the mass transport of oxygen via the oxygen concentration and flow velocity. The fractional heat losses increase from 15 to 30% at high flow velocity to 70% at low flow velocity at the lower oxygen concentrations prior to quenching extinction. Quenching extinction is noted when the heat feedback rate from the leading edge of the flame to the surface is no longer sufficient to offset the ongoing losses, which is estimated to be when heat loss exceeds 70% of the heat feedback rate from the flame.

Despite significant preheating by the upstream flame, the downstream flame is not simultaneously viable because of the 'oxygen

shadow' of the upstream flame for the flow conditions studied in air. Once the upstream spread is complete and extinguished, oxygen penetrates downstream, the downstream flame becomes viable, and cocurrent flame spread is observed. Even with convective preheating, however, the concurrent flame spread is slightly slower than upstream flame spread at a given imposed flow velocity ($<$10 cm/s).

Quenching extinction is noted at very low flows for both upstream and downstream flame spread. The quench regime spans from just below 0.5 cm/s for opposed flow flame spread through quiescence to approximately -1.5 cm/s for cocurrent flame spread. The skewed nature of the quench regime is believed to be because of the augmenting role of diffusion for opposed flow flame spread, versus the canceling effect of diffusion at very low cocurrent flows.

REFERENCES

1. Kashiwagi, T., *Combust. Sci. Tech*. 8:225–236 (1974).
2. Amos, B., and Fernandez–Pello, A. C., *Combust. Sci. Tech*. 62:331–343 (1988).
3. Nakamura, Y., Yamashita, H., Takeno, T., and Kushida, G., *Combust. Flame* 120:34–48 (2000).
4. Olson, S. L., Ferkul, P. V., and T'ien, J. S., *Twenty-Second Symposium (International) on Combustion*, The Combustion Institute, Pittsburgh, PA, 1988, pp. 1213–1222.
5. Olson, S. L., *Combust. Sci. Tech*. 76:233–249 (1991).
6. Kashiwagi, T., McGrattan, K. B., Olson, S. L., Fujita, O., Kikuchi, M., and Ito, K., *Twenty-Sixth Symposium (International) on Combustion*, The Combustion Institute, Pittsburgh, PA, 1996, pp. 1345–1352.
7. Grayson, G. D., Sacksteder, K. R., Ferkul, P. V., and T'ien, J. S., *Microgravity Sci. Technol*. VII/2:187–195 (1994).
8. Di Blasi, C., Crescitelli, S., and Russo, G., *Fire Safety Science—Proceedings of the Second International Symposium*, p. 119–128 (1989).
9. Bhattacharjee, S., and Altenkirch, R. A., *Twenty-Third Symposium (International) on Combustion*, The Combustion Institute, Pittsburgh, PA, 1990, pp. 561–568.
10. Ferkul, P. V., and T'ien, J. S., *Combust. Flame* 99:345–370 (1994).
11. White, K. A., *Ignition of Cellulosic Paper at Low Radiant Fluxes*, NASA TM 107311, August, 1996.
12. McGrattan, K. B., Kashiwagi, T., Baum, H. R., and Olson, S. L., *Combust. Flame* 106:377–391 (1996).
13. Ramachandra, P. A., Altenkirch, R. A., Tang, L., Bhattacharjee, S., and Sacksteder, K., *Combust. Flame* 100:71–84, 1995.
14. T'ien, J. S., Sacksteder, K. R., Ferkul, P. V., Bedir, H., Shih, Hsin-Yi, Greenberg, P. S., Pettigrew, R. D., Piltch, N., and Frate, D., *Fourth Int'l Microgravity Comb. Workshop*, NASA Conference Publication 10194, pp. 399–404 (1997).
15. Dietrich, D. L., Ross, H. D., Frate, D. T., T'ien, J. S., and Shu, Y., *Fourth Int'l Microgravity Comb. Workshop*, NASA Conference Publication 10194, pp. 237–242 (1997).
16. Pettigrew, R., MS Thesis, Case Western Reserve University, May, 1995.
17. Hirano, T., and Sato, K., *Fifteenth Symposium (International) on Combustion*, The Combustion Institute, Pittsburgh, PA, 1974, pp. 233–241.
18. Kashiwagi, T., and Nambu, H., *Combust. Flame*, 88:345–368 (1992).
19. Nakabe, K., McGrattan, K. B., Kashiwagi, T., Baum, H. R., Yamashita, H., and Kushida, G., *Combust. Flame*, 98:361–374 (1994).